공학박사학위논문

The extended bounce-averaged kinetic model for trapped electron mode instability

간힌 전자 모드 불안정성을 위한 확장된 bounce 평균된 운동학적 모델

2022 년 8 월

서울대학교 대학원

에너지시스템공학부

김 용 직

공학박사학위논문

The extended bounce-averaged kinetic model for trapped electron mode instability

간힌 전자 모드 불안정성을 위한 확장된 bounce 평균된 운동학적 모델

2022 년 8 월

서울대학교 대학원

에너지시스템공학부

김 용 직

The extended bounce-averaged kinetic model for trapped electron mode instability

간힌 전자 모드 불안정성을 위한 확장된 bounce 평균된 운동학적 모델

지도교수 함 택 수

이 논문을 공학박사 학위논문으로 제출함

2022 년 8 월

서울대학교 대학원

에너지시스템공학부 원자핵공학전공

김 용 직

김용직의 공학박사 학위논문을 인준함

2022 년 8 월

위 원 장	나용수	(인)
부위원장	함택수	(인)
위 원	황용석	(인)
위 원	이정표	(인)
위 원	윤의성	(인)

Abstract

The extended bounce-averaged kinetic model for trapped electron mode instability

Yong Jik Kim
Department of Energy Systems Engineering
The Graduate School
Seoul National University

The bounce-kinetic model based on the modern nonlinear bounce-kinetic theory has been developed and used for simulations previously. This thesis reports on an extension of the bounce-kinetic model including more accurate treatment of barely trapped particles, and its implementation in the gKPSP gyrokinetic code. The Hamiltonian of trapped particles as a function of adiabatic invariants in bounce-gyrocenter coordinates is derived and the result is verified against the known formula for precession drift. In the gKPSP code, using the extended model leads to more accurate gyrokinetic simulations of Collisionless Trapped Electron Mode (CTEM). In particular, the model shows reduced growth rate in linear simulations at low magnetic shear and lower heat flux and radial electric field in nonlinear simulations of reversed shear plasma. Possible applications of the extended bounce-kinetic model are discussed.

Keywords: fusion plasma, tokamak, turbulence, gyrokinetic simulation, bounce-kinetics, trapped electron mode

Student Number: 2018-26018

Contents

Chapter 1

Introduction

1.1 Motivation

Tokamak plasma is one of the most promising candidates for making fusion energy a reality. Significant efforts have been made so far, including decades of research and various experimental projects, notably the international project ITER, but many challenges remain. Aside from practical difficulties such as engineering limitations and economic feasibility, the underlying physics including turbulent transport still has outstanding questions. In tokamak plasma, particle and heat transport are determined by microturbulence which has time scales comparable to that of drift waves, and their characteristic time is much slower than magnetohydrodynamic (MHD) instabilities which limit equilibrium profiles. To describe fusion plasma microturbulence, wave-particle interaction in the kinetic equations has to be properly treated. Reduced kinetic description based on the nonlinear gyrokinetic formulation [1] and its modern extension keeping the conservation properties intact [2,3] have provided theoretical foundations for studying turbulence. It also led to significant advances in nonlinear gyrokinetic simulations [4,5]. Reduction in the dimensionality of the phase space via decoupling and elimination of the gyrophase dependence for the turbulence phenomena of interest with the characteristic frequency $\omega \ll \Omega_{ci}$ where Ω_{ci} is the ion cyclotron frequency, has been crucial in saving computational time. Numerical gyrokinetic studies have calculated quantitative estimates of the turbulent transport by calculating the linear growth rate and quasilinear flux, often in local δf gyrokinetic simulations which calculate only the local evolution of the perturbed distribution function. However, limitations of the local δf approach have become clear as recent studies have shown that non-diffusive transport processes such as turbulence spreading [6–8] and avalanche-like transport [9–11], and structures resulting from nonlinear interaction of turbulence such as the $E \times B$ staircase [12–14] and transport barriers have a significant impact on transport physics. It is now believed that nonlinear dynamics can have a substantial role in transport, and those require numerical studies of long-time evolution in a closed self-consistent system. To that end, global full-f gyrokinetic codes using flux-driven sources have been developed, but with increased computing power requirements.

1.2 The bounce-kinetic model

Modern nonlinear bounce-kinetics addresses fusion plasma turbulence with its frequency ω much lower than the bounce frequency ω_b, i.e. $\omega \ll \omega_b$ [15,16]. In this formalism, Lie perturbed transforms are used to remove gyrophase dependency and bounce-phase dependency in phase-space Lagrangian. The bounce-kinetic model provides several advantages in numerical simulations with kinetic electron responses. In the model, the kinetic responses from fast electron streaming motions are explicitly removed, which allows us to employ a much longer time step size compared to the typical time steps for simulations based on the conventional drift-kinetic electron model. Also, the model employs the bounce-average operations both in evaluating the source for the Poisson equation and in interpolating electrostatic fields to evolve the kinetic distribution. For particle-in-cell simulations, the bounce-average can reduce noises originating from the discreteness of particles. The bounce-kinetic model has been applied in various codes to study the TEM instability [17–19] achieving promising results comparable to codes using fully kinetic electrons while reducing computing cost significantly. In addition, it provided a very efficient method to extend the Rosenbluth-Hinton residual zonal flow calculation for various applications [16, 20–22].

Regarding the applications to simulations, a bounce-averaged model has been developed for studies on trapped ion modes (TIM) for which both passing ions and passing electrons are assumed to follow Boltzmann response, using a Vlasov code [23]. It has been further extended to address the TIM-driven transport, in particular roles of neoclassical polarization density [15, 24], zonal flows, and the magnetic shear [25]. Idomura et al. have developed the transit averaged reduced kinetic model in a simple geometry [26], and have demonstrated the feasibility of the bounce-kinetic model for TEM studies in tokamak geometry [17]. Later, a bounce-kinetic model has been applied to a linear studies of TIM and TEM [27]. More recently, gKPSP gyrokinetic simulations have used the bounce-kinetic electrons extensively [18, 19] and the details of the model are described in Ref. 19.

1.3 Outline of this dissertation

In this thesis, I provide a bounce-kinetic model that is valid for both barely trapped particles and deeply trapped particles. It is an improvement upon previous bounce-kinetic implementations [18, 19] which use expressions valid only in deeply trapped limit. I derive the "extended model" using modern bounce-kinetics, and then use it for gKPSP gyrokinetic simulations of Collisonless Trapped Electron Mode (CTEM). The new model correctly computes reduced growth rate in weak magnetic shear plasmas due to barely trapped particles' reversed precession, hence provides a more realistic result.

The remainder of this thesis is organized as follows. In Chap. 2, the theoretical model is presented after brief reviews of the modern nonlinear gyrokinetics and bounce-kinetics. Here, formulas for the equilibrium Hamiltonian in deeply trapped and barely trapped limits are derived. The model is verified against the existing theory [28] by deriving precession drift. In Chap. 3, I introduce the implementation of the extended model on the gKPSP gyrokinetic code and the results from linear and nonlinear CTEM simulations. I compare the results from the old bounce-kinetics model and the extended model to highlight the advantages of the extended model. In Chap. 4, I discuss possible applications and future works of the extended model. In Chap. 5, I summarize the findings and conclude the thesis.

Chapter 2

Theoretical model

2.1 Modern nonlinear gyrokinetics

In this section, I introduce the modern nonlinear gyrokinetics which set the basis of the modern bounce-kinetics. Nonlinear gyrokinetics provides a framework that can describe the kinetic effects of fully ionized plasmas in a strong magnetic field, such as tokamak plasmas. One of the central motives of gyrokinetics is to reduce dimensionality while conserving relevant physics. In tokamak plasmas, turbulent transport dictates energy confinement, and its characteristic time is much longer than that of MHD instability or Larmor gyration. Thus, plasma particles' fast gyro-motion can be ignored, as long as one properly treats the spatial effects of gyro-motion, often referred to as the finite Larmor radius (FLR) effect. This is not a trivial task as both non-perturbed physical quantities such as the background magnetic field and the perturbation fields vary with gyro-phase.

The earliest derivation of nonlinear gyrokinetics by Frieman and Chen [1] did not explicitly satisfy conservation laws such as conservation of total energy and momentum. This can lead to inaccurate results in long-time studies, such as non-physical dissipation in the numerical analysis. In the modern nonlinear gyrokinetics first introduced by Hahm [2], a more sophisticated approach involving Lie perturbation theory [29, 30] is used. In the modern formalism, Lagrangian 1-form Γ in non-canonical particle coordinate $(\mathbf{x}, \mathbf{v})$ transforms to gyrocenter (gy) coordinates which eliminate gyrophase dependency in phase space Lagrangian 1-form $\overline{\Gamma}$ to the second order of $\epsilon_\phi = e\phi/T$, the small parameter of perturbation scales. Mathematically, it is written as $\overline{\Gamma} = T_{\mathrm{gy}}^{-1}\Gamma + dS$. Here, T_{gy}^{-1} is the push-forward operator and dS is the gauge term. By requiring that the first and the second order of $\overline{\Gamma}$ is independent of gyro-phase, all the terms in T_{gy}^{-1} and S can be explicitly obtained up to the second order. From here, one now has all the ingredients of the self-consistent gyrokinetic system, gyrokinetic Vlasov and Poisson-Ampere equations which have been widely used in numerical and theoretical studies.

2.2 Outline of bounce-kinetic theory

Further reduction of dimensionality is possible if one considers time scale much slower than trapped particle bounce frequency so that $\omega \ll \omega_b$. This leads to bounce-kinetic equations which now have two ignorable quantities, gyro-phase and bounce-phase. Based on the modern gyrokinetic framework summarized in Sec. 2.1, Fong and Hahm [15] have derived bounce-kinetic Vlasov and Poisson equations. They start their derivation from gy coordinates, where gyrocenter position is now a function of (α, β, s) where $\alpha \equiv \varphi - q\theta$ is an angle coordinate along the binormal direction, φ is the toroidal angle, θ is the poloidal angle, and q is the safety factor. $\beta \equiv \psi(r)$ is the poloidal flux, $s \equiv qR_0\theta$ is the distance along the magnetic field, and R_0 is the major radius. Next, gyrocenter coordinates transform to bounce-guiding center (bgc) coordinates where bounce angle dependency is eliminated in phase-space Lagrangian at the lowest order of ϵ_ϕ. Further transformation eliminates bounce angle dependency in phase-space Lagrangian to the second order in ϵ_ϕ, and finally one is left with bounce-gyrocenter (bgy) coordinates. Assuming electrostatic perturbations, Lagrangian 1-form Γ and the Hamiltonian H in bgy coordinates are written as [15]

$$\begin{aligned} \Gamma &= \frac{e}{c} + J_b d\Psi - H_0(\alpha, \beta, J_b)dt - e\phi_{\text{eff}}(\alpha, \beta, J_b)dt \\ &= \frac{e}{c} + J_b d\Psi - H dt, \\ H &= H_0 + \delta H = H_0(\alpha, \beta, J_b) + e\phi_{\text{eff}}(\alpha, \beta, J_b). \end{aligned} \tag{2.1}$$

where Ψ is the bounce phase, H_0 is the equilibrium Hamiltonian, $\delta H = H - H_0$ is the perturbed Hamiltonian, and ϕ_{eff} is the effective potential in bgy coordinates. Note that from Eq. 2.1 and onwards, α and β correspond to the binormal angle coordinate and the poloidal flux written in bgy coordinates respectively. The Hamilton's equations in bgy coordinates are given as follows.

$$\begin{aligned} \frac{d\beta}{dt} &= \frac{c}{e}\frac{\partial \delta H}{\partial \alpha} \\ \frac{d\alpha}{dt} &= -\frac{c}{e}\frac{\partial H_0}{\partial \beta} - \frac{c}{e}\frac{\partial \delta H}{\partial \beta} \\ \frac{dJ}{dt} &= -\frac{\partial H}{\partial \Psi} = 0 \\ \frac{d\Psi}{dt} &= \frac{\partial H}{\partial J} \end{aligned} \tag{2.2}$$

Pitch angle κ is defined as

$$\kappa^2 \equiv \frac{v_{\|0}^2}{2\epsilon v_{\perp 0}^2} \tag{2.3}$$

where $v_{\|0}$ and $v_{\perp 0}$ are parallel and perpendicular velocities at the outmost mid-plane of the particle orbit, respectively. In a high aspect ratio tokamak

($\epsilon = a/R_0 \ll 1$), bounce frequency ω_b and bounce action $J_b \equiv \oint v_\parallel dl$ are given as [16]

$$\begin{aligned} J_b &= \frac{8}{\pi} q R_0 \sqrt{\epsilon m \mu B_0}[E(\kappa) - (1-\kappa^2)K(\kappa)] \\ \omega_b &= \frac{1}{qR_0}\sqrt{\frac{\epsilon \mu B_0}{m}}\frac{\pi}{2K(\kappa)} \end{aligned} \tag{2.4}$$

where $K(\kappa)$ and $E(\kappa)$ are complete elliptic integrals of the first kind and the second kind, respectively, defined as follows.

$$\begin{aligned} E(\kappa) &\equiv \int_0^{\pi/2} \sqrt{1-\kappa^2 \sin^2\theta} \\ K(\kappa) &\equiv \int_0^{\pi/2} \frac{d\theta}{\sqrt{1-\kappa^2\sin^2\theta}} \end{aligned} \tag{2.5}$$

The definition of bounce frequency, in terms of action-angle invariant J_b is

$$\omega_b = \frac{\partial H_0}{\partial J_b} \tag{2.6}$$

and therefore

$$H_0 = \int \omega_b dJ_b. \tag{2.7}$$

For the remainder of this thesis, I refer to the equilibrium Hamiltonian simply "Hamiltonian". To date, deeply trapped approximation ($J_b \sim 0$) has been widely used to express Hamiltonian as $H_0 \simeq H_{0,init} + \omega_b J_b$, where $H_{0,init}$ is an initial value of Hamiltonian in the $J_b = 0$ limit, for bounce-kinetics applications [17–19].

In this work, I focus on trapped electron dynamics and deal with Hamiltonian of trapped particles. To solve the equations of motion shown in Eq. 2.2, one has to know the exact expression of H_0 in terms of α, β, μ, and J_b. However, in the literature, such a formula is not readily available except for deeply trapped particles, while Eq. 2.4 is well-known. In this thesis, I derive such expression for barely trapped particles and use it for the extended bounce-kinetic model.

The remainder of this chapter is organized as follows. In Sec. 2.3, I introduce a systematic way to derive the Hamiltonian in terms of bounce action J_b, and present a model that can accurately describe the dynamics of both deeply trapped and barely trapped particles. This is done by writing Hamilton's equation in deeply trapped and barely trapped limits and making a connection formula. In Sec. 2.4, I verify the model by calculating precession frequency from the equations of motion and compare it with the well-known results [28].

2.3 Hamiltonian in bounce-gyrocenter coordinates

With flux coordinates and magnetic moment fixed, the Taylor expansion of the Hamiltonian in bounce action J_b around $J_b = 0$ is written as

$$H_0(J_b) = H_0(0) + \left.\frac{\partial H_0}{\partial J_b}\right|_{J_b=0} J_b + \frac{1}{2}\left.\frac{\partial^2 H_0}{\partial J_b^2}\right|_{J_b=0} J_b^2 + \cdots . \tag{2.8}$$

For deeply trapped particles, this method is valid and the coefficients in Eq. 2.8 are derived from parametric derivatives in which J_b and ω_b are expressed in terms of κ as given in Eq. 2.4. Approximations of complete elliptic integrals at $\kappa \ll 1$ are as follows [16]:

$$\begin{aligned} E(\kappa) &= \frac{\pi}{2}\left(1 - \sum_{n=1}^{\infty}\left(\frac{1\cdot 3\cdots(2n-1)}{2\cdot 4\cdots 2n}\right)^2 \frac{\kappa^{2n}}{2n-1}\right) \\ &= \frac{\pi}{2}\left(1 - \frac{\kappa^2}{4} - \frac{3}{64}\kappa^4 + \cdots\right) \end{aligned} \tag{2.9}$$

$$\begin{aligned} K(\kappa) &= \frac{\pi}{2}\left(1 + \sum_{n=1}^{\infty}\left(\frac{1\cdot 3\cdots(2n-1)}{2\cdot 4\cdots 2n}\right)^2 \kappa^{2n}\right) \\ &= \frac{\pi}{2}\left(1 + \frac{\kappa^2}{4} + \frac{9}{64}\kappa^4 + \cdots\right) \end{aligned} \tag{2.10}$$

The expansions of J_b and ω_b are then given as [31]

$$\begin{aligned} J_b &\simeq 2qR_0\sqrt{m\epsilon\mu B_0}\left(\kappa^2 + \frac{\kappa^4}{8} + \cdots\right), \\ \omega_b &\simeq \frac{1}{qR_0}\sqrt{\frac{\epsilon\mu B_0}{m}}\left(1 - \frac{\kappa^2}{4} - \cdots\right). \end{aligned} \tag{2.11}$$

Using these expressions, coefficients of the Hamiltonian are given as

$$\begin{aligned} \left.\frac{\partial H_0}{\partial J_b}\right|_{J_b=0} &= \omega_b|_{\kappa=0} = \frac{1}{qR_0}\sqrt{\frac{\epsilon\mu B_0}{m}}, \\ \left.\frac{\partial^2 H_0}{\partial J_b^2}\right|_{J_b=0} &= \left.\frac{\partial\omega_b(\kappa)/\partial\kappa}{\partial J_b(\kappa)/\partial\kappa}\right|_{J_b=0} = \frac{1}{2m(qR_0)^2}\left.\frac{-\frac{1}{2}\kappa - \cdots}{2\kappa + \frac{1}{2}\kappa^3 + \cdots}\right|_{\kappa=0} \\ &= -\frac{1}{8m(qR_0)^2}. \end{aligned} \tag{2.12}$$

Then, the Hamiltonian is

$$h_{\text{deeply}}(\mu, J_b) = \mu B_{om} + \frac{\sqrt{\epsilon\mu B_0}}{qR_0\sqrt{m}}J_b - \frac{1}{16m(qR_0)^2}J_b^2. \tag{2.13}$$

Here, B_{om} is the magnetic field at the outer most mid-plane of the particle orbit. Note that in the Hamiltonian, ϵ and q have explicit dependencies on β, while J_b is an independent variable.

A different approach should be taken for barely trapped particles. For them, J_b can not assumed to be small when compared to μB_{om}, and $\partial\omega_b/\partial J_b$ diverges at $\kappa = 1$ so Taylor expansion of H_0 around $\kappa = 1$ is not valid. For barely trapped particles, I start from asymptotic formulas of J_b and ω_b, and write J_b as a function of ω_b. Then, I integrate ω_b as given in Eq. 2.7. For $\kappa' \ll 1$, where $\kappa'^2 = 1 - \kappa^2$, complete elliptic integrals can be approximated as:

$$E(\kappa) \simeq 1 + \frac{\kappa'^2}{2}\left(\log\frac{4}{\kappa'} - \frac{1}{2}\right), \tag{2.14}$$

$$K(\kappa) \simeq \log\frac{4}{\kappa'}\left(1 + \frac{\kappa'^2}{4}\right) - \frac{\kappa'^2}{24}. \tag{2.15}$$

Therefore, asymptotic formulas of J_b and ω_b are

$$\begin{aligned} J_b &\simeq \frac{8}{\pi} q R_0 \sqrt{m\mu\epsilon B_0}\left(1 - \frac{\kappa'^2}{4} - \frac{\kappa'^2}{2}\log\frac{4}{\kappa'}\right) \\ &\simeq J_{b*}\left(1 - \frac{\kappa'^2}{4}\log\frac{16}{\kappa'^2}\right) \end{aligned} \tag{2.16}$$

$$\omega_b \simeq \frac{\pi}{2qR_0}\sqrt{\frac{\epsilon\mu B_0}{m}}\frac{1}{\log\dfrac{4}{\kappa'}} = \frac{\omega_{b*}}{\log\dfrac{16}{\kappa'^2}} \tag{2.17}$$

where $J_{b*} = \dfrac{8}{\pi} q R_0 \sqrt{m\mu\epsilon B_0}$ and $\omega_{b*} = \dfrac{\pi}{qR_0}\sqrt{\dfrac{\epsilon\mu B_0}{m}}$. This leads to

$$\omega_b = -\omega_{b*}\frac{1}{W_m\left(\dfrac{1}{4}\left(\dfrac{J_b}{J_{b*}} - 1\right)\right)} \tag{2.18}$$

where $W_m(x)$ denotes the second branch of Lambert function which is defined by $W(x)e^{W(x)} \equiv x$ for $W(x) < -1$ (Fig. 2.1. [32]. Then, H_0 in terms of J_b is given as:

$$h_{\text{barely}}(\mu, J_b) = \mu B_{im} + 4\omega_{b*} J_{b*} \int_0^{(1/4)(1-J_b/J_{b*})} \frac{dt}{W_m(-t)} \tag{2.19}$$

Here, B_{im} is the magnetic field at the innermost mid-plane of the particle orbit. Note that the first term is the particle energy of the marginally trapped particle at the limit $\kappa = 1$. Also, note that the second term has a minus sign.

One can derive Hamiltonian and respective Hamilton's equations for barely passing ($\kappa'^2 = \kappa^2 - 1 \ll 1$) and strongly passing particles ($\kappa^2 \gg 1$) using the same procedures from this section. In other words, the same methodology can be applied to expand J_t and ω_t, then obtain H_0 as a function of J_t. Here, t stands for "transit".

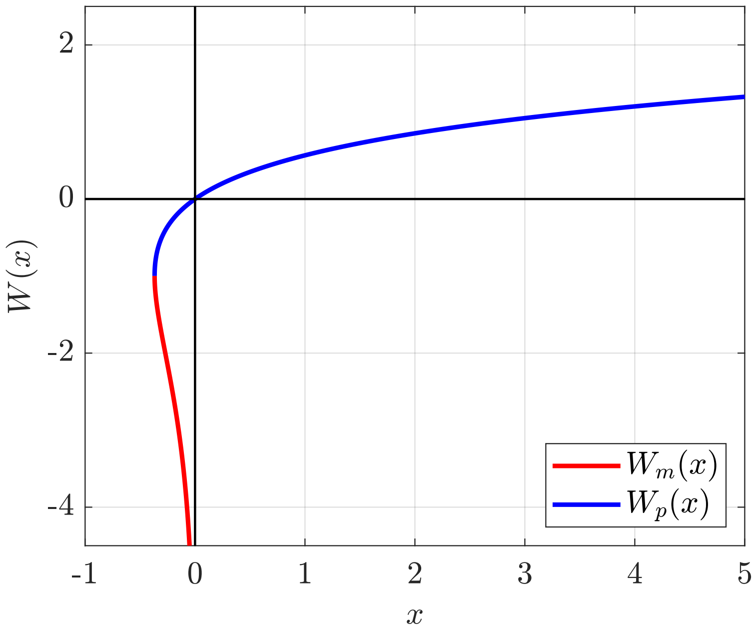

Figure 2.1 Two branches of the Lambert function $W_m(x)$ in blue and $W_p(x)$ in red [32].

2.4 Precession drift

In tokamak plasmas, background magnetic field is inhomogeneous and this leads to bounce motion of particles as I discussed in the Sec. 2.3. Inhomogenous magnetic field results in a drift motion which direction is binormal to both radial direction and magnetic field line direction. This is called precession drift, and in this thesis the precession drift corresponds to a drift motion along α coordinate. Precession drift's analytic expression is well known since Kadomtsev and Pogutse's paper from 1967 [28] and can be derived explicitly using orbit averaging [33]. Here, I derive precession drift in the context of modern bounce-kinetic formalism, i.e., directly from differentiation of Hamiltonian with respect to the second adiabatic invariant J_b. This can be done with our result from Eqs. 2.13 and 2.19 in deeply trapped and barely trapped limits. In this section, I verify the results from the extended model by comparing it with Kadomtsev and Pogutse's formula.

According to Kadomtsev and Pogutse, precession drift frequency $\langle\omega_{dj}\rangle_b$ of a species j is expressed as follows:

$$\begin{aligned}\langle\omega_{dj}\rangle_b &= \omega_{*j}\frac{L_{nj}E_0}{R_0T_j}G(\hat{s},\kappa) = -k_\theta\frac{cT_j}{Z_jeBL_{nj}}\frac{L_{nj}E_0}{R_0T_j}G(\hat{s},\kappa) \\ &= -\frac{ck_\theta E_0}{Z_jeBR_0}G(\hat{s},\kappa) \qquad (2.20)\end{aligned}$$

$$\text{where } G(\hat{s},\kappa) = 2\frac{E(\kappa)}{K(\kappa)} - 1 + 4\hat{s}\left(\frac{E(\kappa)}{K(\kappa)} + \kappa^2 - 1\right).$$

For electrons Eq. 2.20 can be simplified as $\langle\omega_{de}\rangle_b = \overline{\omega}_{de}G(\hat{s},\kappa)$ with $\overline{\omega}_{de} = \dfrac{ck_\theta E_0}{eBR_0}$. Here, E_0 is the particle energy. The G function is plotted in Fig. 2.2. The sign of G function indicates precession direction of trapped particles. For most positive magnetic shear values, G is positive for all κ. For weak magnetic shear $\hat{s} \simeq 0$, precession reversal of barely trapped particles ($\kappa \simeq 1$) starts to

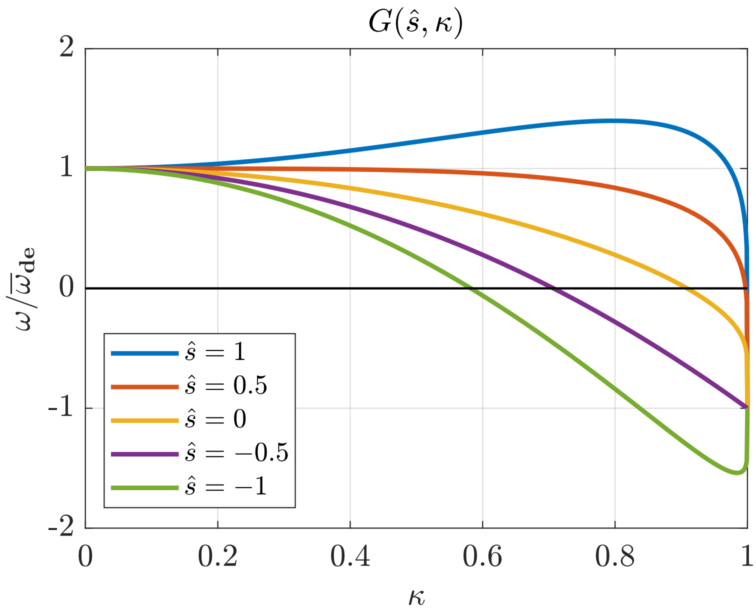

Figure 2.2 $G(\hat{s}, \kappa)$ function [28] plotted in terms of κ for different magnetic shear $\hat{s}$ values. Sign of function G determines precession direction.

occur. For negative magnetic shear (for instance, $\hat{s} = -1$) as shown in Fig. 2.2, precession reversal happens at wide range of κ values, thus its impact can be significant. This $\hat{s}$ dependence of G is important for TEM as it is destabilized by the precession of trapped electrons in the electron diamagnetic drift direction. Therefore, TEM drive gets weaker as magnetic shear decreases, especially when barely trapped particle fraction is high.

Now, I derive the precession drift from the extended model. First, I consider deeply trapped particles ($\kappa \ll 1$). Using the approximations for elliptic integrals given in Eqs. 2.14 and 2.15, I write

$$\frac{E(\kappa)}{K(\kappa)} \simeq \frac{1 - \dfrac{\kappa^2}{4} - \dfrac{3}{64}\kappa^4}{1 + \dfrac{\kappa^2}{4} + \dfrac{9}{64}\kappa^4} = 1 - \frac{1}{2}\kappa^2 - \frac{1}{16}\kappa^4 + O(\kappa^6). \tag{2.21}$$

Then, $G(\hat{s}, \kappa)$ is approximated as

$$G(\hat{s}, \kappa) \simeq 1 - \kappa^2 - \frac{1}{8}\kappa^4 + \hat{s}\left(2\kappa^2 - \frac{\kappa^4}{4}\right). \tag{2.22}$$

Partial derivative of Hamiltonian for deeply trapped particles h_{deeply} (Eq. 2.13) in radial direction is

$$\begin{aligned} \frac{\partial h_{\text{deeply}}}{\partial r} &= -\frac{\mu B_0}{R_0} + \frac{1}{2}\frac{1}{qR_0^2}\sqrt{\frac{\mu B_0}{m\epsilon}}J_b - \frac{\sqrt{\epsilon \mu B_0}}{qrR_0\sqrt{m}}\hat{s}J_b + \frac{\hat{s}}{8mq^2R_0^2 r}J_b^2 \\ &\simeq \frac{\mu B_0}{R_0}\left[-1 + \kappa^2 + \frac{\kappa^4}{8} - \hat{s}\left(2\kappa^2 - \frac{\kappa^4}{4}\right)\right] \\ &= -\frac{\mu B_0}{R_0}G_{\text{deeply}}. \end{aligned} \tag{2.23}$$

Here, I used $J_b \simeq 2qR_0\sqrt{m\epsilon\mu B_0}(\kappa^2 + \kappa^4/8) + O(\kappa^6)$.

The derivation of Hamiltonian for barely trapped particles follows similar steps. For barely trapped particles with $\kappa'^2 \equiv 1 - \kappa^2 \ll 1$, I write

$$\frac{E(\kappa)}{K(\kappa)} \simeq \frac{1 + \dfrac{\kappa'^2}{2}\left(\log\dfrac{4}{\kappa'} - \dfrac{1}{2}\right)}{\log\dfrac{4}{\kappa'}} \simeq \frac{\kappa'^2}{2} + \frac{1}{\log\dfrac{4}{\kappa'}} \tag{2.24}$$

and

$$G(\hat{s}, \kappa) \simeq -1 + \kappa'^2 + \frac{2}{\log\dfrac{4}{\kappa'}} + 4\hat{s}\left(-\frac{\kappa'^2}{2} + \frac{1}{\log\dfrac{4}{\kappa'}}\right) \tag{2.25}$$

with expansions up to $O(\kappa'^2)$ and $O(\log^{-1}\kappa')$. To obtain precession drift from Hamiltonian, I use the following identity:

$$\int \frac{dx}{W_m(-x)} = \mathrm{E}_1(-W_m(-x)) + \frac{x}{W_m(-x)} + C, \tag{2.26}$$

where $\mathrm{E}_1(x) \equiv \int_x^\infty u^{-1}e^{-u}du$ is the exponential integral function, and C is some constant. The integral term in Hamiltonian (Eq. 2.19) is now simplified as

$$\int_0^{(1/4)(1-J_b/J_{b*})} \frac{dt}{W_m(-t)} = \mathrm{E}_1\left(2\log\frac{4}{\kappa'}\right) - \frac{\kappa'^2}{16}. \tag{2.27}$$

Then, the radial partial derivative of the Hamiltonian for barely trapped particles h_{barely} (Eq. 2.19) is

$$\begin{aligned}\frac{\partial h_{\text{barely}}}{\partial r} =& \frac{\mu B_0}{R_0} + \frac{32\mu B_0}{R_0}\left(E_1\left(2\log\frac{4}{\kappa'}\right) - \frac{\kappa'^2}{16}\right) \\ &- \frac{2\mu B_0}{R_0}(2+4\hat{s})\left(\frac{1}{2\log\frac{4}{\kappa'}} - \frac{\kappa'^2}{4}\right) \\ =& -\frac{\mu B_0}{R_0}G_{\text{barely}}.\end{aligned} \tag{2.28}$$

Using asymptotic formula $E_1(x) \simeq xe^{-x}$, Eq. 2.28 up to $O(\kappa'^2)$ and $O(\log^{-1}\kappa')$ is written as

$$\begin{aligned}\frac{\partial h_{\text{barely}}}{\partial r} \simeq& \frac{\mu B_0}{R_0} + \frac{\mu B_0}{R_0}\left(\frac{\kappa'^2}{\log\frac{4}{\kappa'}} - 2\kappa'^2\right) \\ &- \frac{2\mu B_0}{R_0}(2+4\hat{s})\left(\frac{1}{2\log\frac{4}{\kappa'}} - \frac{\kappa'^2}{4}\right) \\ \simeq& \frac{\mu B_0}{R_0}\left[1 - \kappa'^2 - \frac{2}{\log\frac{4}{\kappa'}} - \hat{s}\left(\frac{4}{\log\frac{4}{\kappa'}} - 2\kappa'^2\right)\right].\end{aligned} \tag{2.29}$$

From Hamilton's equations Eqs. 2.23 and 2.29, the precession drift is obtained as follows.

$$\frac{d\alpha}{dt} \simeq \begin{cases} -\frac{c}{e}\frac{\mu B_0}{RR_0B_p}\left[1 - \kappa^2 - \frac{\kappa^4}{8} + \hat{s}\left(2\kappa^2 - \frac{\kappa^4}{4}\right)\right] & \text{if } \kappa \ll 1 \\ -\frac{c}{e}\frac{\mu B_0}{RR_0B_p}\left[-1 + \kappa'^2 + \frac{2}{\log\frac{4}{\kappa'}} + \hat{s}\left(\frac{4}{\log\frac{4}{\kappa'}} - 2\kappa'^2\right)\right] & \text{if } \kappa' \ll 1 \end{cases} \tag{2.30}$$

By comparing Eqs. 2.22, 2.25 and 2.30, it's evident that precession drift calculated from the extended model is consistent with Kadomtsev and Pogutse's formula as $\langle\omega_{de}\rangle_b = \langle \mathbf{v}_{de}\cdot\mathbf{k}_\perp\rangle_b \simeq -k_\theta \frac{r}{q}\frac{d\alpha}{dt} \simeq \overline{\omega}_{de}G(\hat{s},\kappa)$ in both limits. It should be noted that Eq. 2.29 is a more crude approximation than Eq. 2.28, and it is only mentioned for comparison with Eq. 2.25. I will be using Eq. 2.28, i.e., G_{barely} to assess the accuracy of the extended model. In Fig. 2.3, $\omega/\overline{\omega}_{de}$ against $G(\hat{s},\kappa)$ is plotted using Eq. 2.30. In the figure, the extended model's approximations fit $G(\hat{s},\kappa)$ function very well in the respective limits. Furthermore, a connection formula can be constructed as G_{con} (Eq. 2.31) which approximates $G(\hat{s},\kappa)$ from Kadomtsev and Pogutse well for all κ in $0 \leq \kappa \leq 1$ and in wide range of $\hat{s}$ in $-1 < \hat{s} < 1$, as shown in Fig. 2.3.

$$G_{\text{con}} = \left[1 - \left(\frac{J_b}{J_{b*}}\right)^2\right] G_{\text{deeply}} + \left(\frac{J_b}{J_{b*}}\right)^2 G_{\text{barely}} \tag{2.31}$$

Here, J_b is given by Eq. 2.4 with no approximations used for $E(\kappa)$ and $K(\kappa)$.

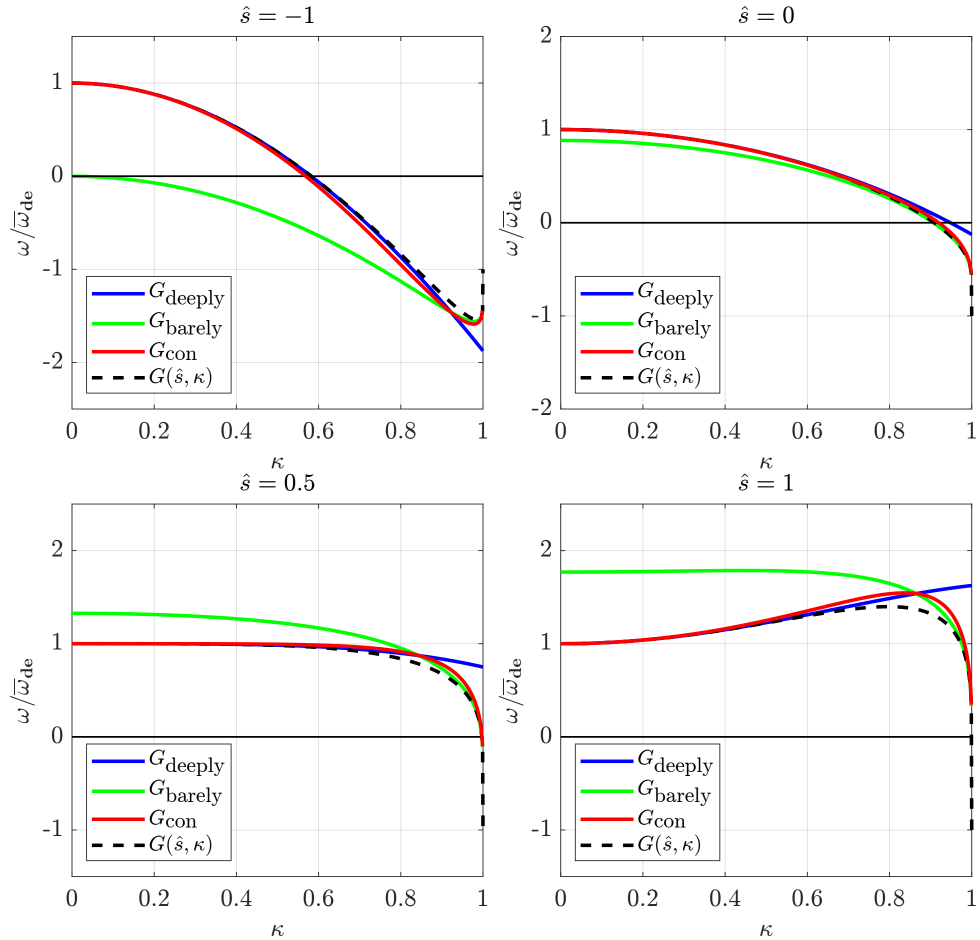

Figure 2.3 Precession drift obtained using deeply trapped approximation (G_{deeply}) in blue line, using barely trapped approximation in green line (G_{barely}) and using connection formula in red line (G_{con}) as given in Eqs. 2.23, 2.28, and 2.31. Three results are compared with $G(\hat{s}, \kappa)$ from Kadomtsev and Pogutse [28] in black dotted line, at magnetic shear $\hat{s} = -1, 0, 0.5$ and 1.

Chapter 3

Extended bounce-kinetic model for trapped electron mode simulations

In this chapter, I implement the extended model in the gKPSP code and apply it in TEM studies, in particular for weak magnetic shear. I describe the numerical model of the bounce-kinetics used in gKPSP in Sec. 3.1, then discuss the linear simulation results in Sec. 3.2 and the nonlinear simulation results in Sec. 3.3.

3.1 Implementation of bounce-kinetic model in gyrokinetic simulation

gKPSP is a global δf gyrokinetic particle-in-cell (PIC) code [34] which has been used to study various topics of turbulent transport physics [18, 35, 36]. The implementation of the bounce-kinetic model for ion temperature gradient-trapped electron mode (ITG-TEM) turbulence in the gKPSP code can be found in Kwon et al. [19]. In its numerical scheme, ions follow the usual nonlinear gyrokinetic equations [2] with Coulomb collisions. Trapped electrons and passing electrons are handled separately. Equation 3.1 is used to describe the evolution of trapped electron distribution function f_e^T,

$$\frac{\partial}{\partial t} f_e^{P,\,T} + \frac{d\mathbf{X}}{dt} \cdot \frac{\partial}{\partial \mathbf{X}} f_e^{P,\,T} + \frac{dv_\parallel}{dt} \frac{\partial}{\partial v_\parallel} f_e^{P,\,T} = C_L(f_e^{P,\,T}) + S_e + S^{P,\,T}. \quad (3.1)$$

Here, S^P is the flux of electrons from being trapped to passing, and S^T is the opposite. $\mathbf{X}$ is the guiding center position and $v_\parallel$ is the parallel velocity of the guiding center. S_s denotes the external source term required to maintain equilibrium profiles for electrons. The bounce-averaged distribution function $F_e \equiv \langle f_e^T \rangle_b$, which represents the distribution function of bounce-gyrocenters, follows bounce-kinetic equations as follows.

$$\frac{\partial F_e}{\partial t} + \frac{d\beta}{dt}\frac{\partial F_e}{\partial \beta} + \frac{d\alpha}{dt}\frac{\partial F_e}{\partial \alpha} = \langle C_L \rangle_b + \langle S_e \rangle_b + \langle S^T \rangle_b, \quad (3.2)$$

$$\begin{aligned} \frac{d\beta}{dt} &= c\frac{\partial \langle \phi \rangle_b}{\partial \alpha} \\ \frac{d\alpha}{dt} &= -\frac{c}{e}\frac{\partial H_0}{\partial \beta} - c\frac{\partial \langle \phi \rangle_b}{\partial \beta}. \end{aligned} \quad (3.3)$$

Here, C_L is the Lorentz collision operator used to model Coulomb collisions of electrons against ions, with $C_L(f_e^{P,\,T}) = \frac{\nu_e}{2}\frac{\partial}{\partial \lambda}(1-\lambda^2)\frac{\partial}{\partial \lambda} f_e^{P,\,T}$, and ϕ is the perturbed electric potential. Note that Eq. 3.3 is an example of Eq. 2.2 with $\delta H = -e\langle \phi \rangle_b$. Distribution function for species s is decomposed as $f_s = f_{s0} + \delta f_s$. Here, f_{s0} is a Maxwellian distribution function, and the evolution of the perturbed distribution function δf_s is obtained from

$$\left(\frac{\partial}{\partial t} + \frac{d\mathbf{z}}{dt} \cdot \frac{\partial}{\partial \mathbf{z}}\right)\delta f_s = -\left.\frac{d\mathbf{z}}{dt}\right|_1 \cdot \frac{\partial}{\partial \mathbf{z}} f_{s0} + C_s + S_s. \quad (3.4)$$

where C_s is the collision term for species s, $\mathbf{z}$ represents phase-space variables for each species, and $d\mathbf{z}/dt|_1$ stands for the terms in the equations of motion for particles containing the electric potential ϕ. This scheme uses drift-kinetic model in Eq. 3.1 for passing electrons. In gKPSP, the passing electrons passively evolve according to the perturbed electric potential, which is self-consistently determined by the ion and trapped electron distribution functions. Without a careful treatment, this approach could lead to a violation of the ambipolar condition. Ref. 37 has demonstrated that such problem can be avoided by using the hybrid kinetic electron model. In bounce-kinetic model implemented in gKPSP, to ensure ambipolarity, the passing electron motions are accurately followed in a sub-cycling way according to Eq. 3.1, except their weights to determine the perturbed distribution δf_e^P is set as adiabatic i.e., $\delta f_e^P = (\phi - \langle\phi\rangle_Z) f_{e0}/T_e$. Here, $\langle\phi\rangle_Z$ denotes the zonal component of the electrostatic potential. In other words, Eq. 3.1 for f_e^P is used to describe the positions and velocities of the simulation marker particles for passing electrons, while the δf_e^P weights of the particles are set as adiabatic. This feature of gKPSP is demonstrated in Fig. 6-(a) of Ref. 19. The evolution of the passing electrons is required to account for the particle fluxes crossing the trapped-passing boundaries and evaluate $S^{P,\,T}$ (see Ref. 19 for details).

As mentioned, the Hamiltonian used in Ref. 19 is $H_0 = \mu B_{om} + \dfrac{\sqrt{\epsilon\mu B_0}}{qR_0\sqrt{m_e}} J_b$, where m_e is the electron mass, which is valid only for deeply trapped electrons. Despite its limitation, it has been used for all trapped electrons in Ref. 19, both deeply trapped and barely trapped. Improving upon this old model, I now use the extended model as given by Eqs. 2.13 and 2.19. Checking if a trapped particle is deeply trapped or barely trapped whenever simulation solves equation of motion of a particle, can lead to numerical issues such as ambiguity in setting deeply trapped and barely trapped boundary, and discontinuity in precession drift as a function of κ. For this reason, in the extended model, I construct a connection formula of the derivative of Hamiltonian in a similar fashion as

Eq. 2.31 as follows:

$$\frac{\partial H_0}{\partial \psi} \simeq \left[1 - \left(\frac{J_b}{J_{b*}}\right)^2\right] \frac{\partial h_{\text{deeply}}}{\partial \psi} + \left(\frac{J_b}{J_{b*}}\right)^2 \frac{\partial h_{\text{barely}}}{\partial \psi}. \tag{3.5}$$

Here, as in Eq. 2.31, J_b is given by Eq. 2.4 with no approximations used for $E(\kappa)$ and $K(\kappa)$. Since the connection formula for G_{con} (Eq. 2.31) achieved high accuracy for all κ as shown in Fig. 2.3, the connection formula for $\frac{\partial H_0}{\partial \psi}$ from Eq. 3.5 also accurately describe all trapped particles in the extended bounce-kinetic model of gKPSP simulation.

3.2 Linear gyrokinetic simulation results

I first apply the extended model using so-called "Cyclone" parameters [38] for ITG-TEM linear simulations. I assume collisionless plasma with minor and major radius $a = 0.48\ m$ and $R_0 = 1.3\ m$, respectively. Other parameters are set as $R_0/L_{ne} = R_0/L_{ni} = 2.22$, $R_0/L_{Ti} = 6.92$, $R_0/L_{Te} = 6.92$, $\hat{s} = 0.8$, and $q = 1.4$. Here, $L_{ns} = -\left(\frac{1}{n_s}\frac{dn_s}{dr}\right)^{-1}$ and $L_{Ts} = -\left(\frac{1}{T_s}\frac{dT_s}{dr}\right)^{-1}$ are density gradient length and temperature gradient length of species s, respectively. I set the time step size as $\Delta t = 0.05\ R_0/v_{Ti}$ and the number of marker particles for trapped electrons as $N_p = 6000$. Simulation results of the linear growth rate and real frequency of the instability, compared with the results from the Gyrokinetic Toroidal δf 3D (GT3D) particle code and Gyrokinetic Toroidal Code (GTC) [39], are given in Fig. 3.1.

As shown in Fig. 3.1, all four simulations—GT3D, GTC, gKPSP using the old model, and gKPSP using the extended model—show a similar trend in real frequency and in growth rate. For real frequency ω_r, the plus sign corresponds to electron diamagnetic direction and the minus sign corresponds to ion diamagnetic direction. For all four cases, real frequency increases linearly with negative

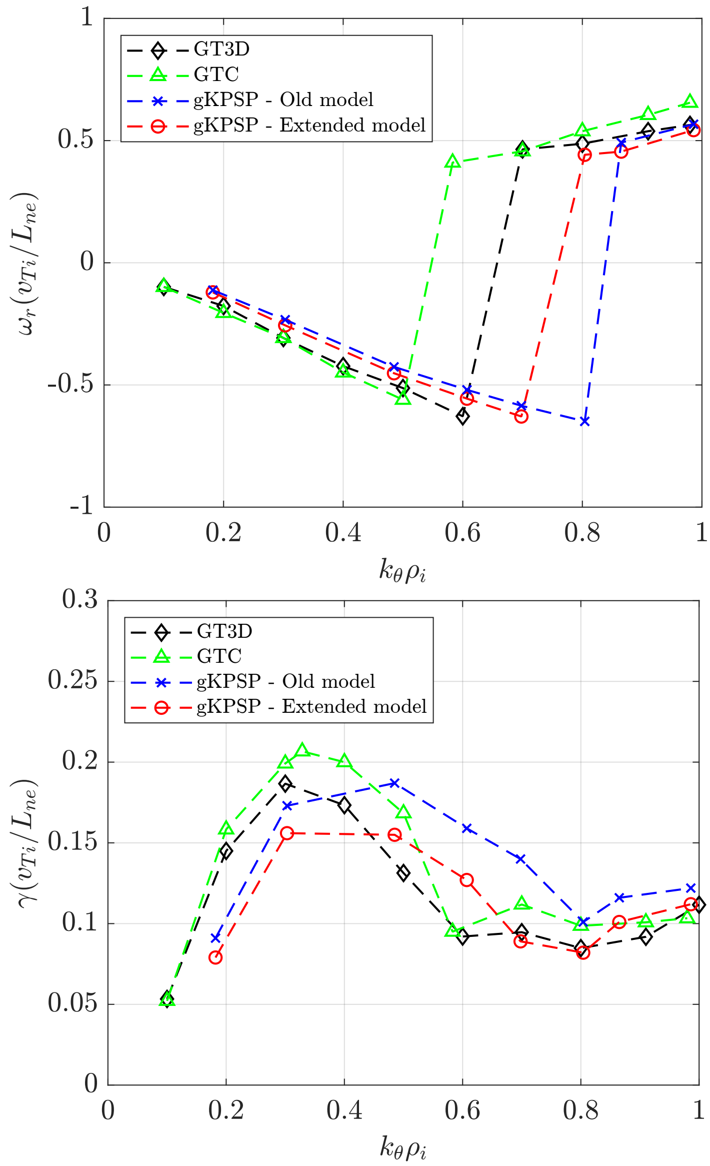

Figure 3.1 Benchmark of the gKPSP code using the extended model for real frequency ω_r and growth rate γ result compared to those from GT3D, GTC, and gKPSP using the old model [19, 39].

sign below some $k_\theta\rho_i$ threshold, and after that the sign is reversed to positive. This means that at a long wavelength, ITG is the dominant instability mode and at a short wavelength TEM is dominant. The transition value of $k_\theta\rho_i$ for gKPSP, at which ITG $\longleftrightarrow$ TEM transition occurs, was higher than those for GT3D and GTC, and the extended model's threshold was lower than the old model. This result suggests that gKPSP using the extended model yields closer results to those from GT3D and GTC which use fully kinetic electrons, compared to the old model. For the growth rate, maximum values at ITG-unstable $k_\theta\rho_i$ region were similar across four results with $\gamma = 0.15 \sim 0.2$. In gKPSP, the extended model shows decrease in the growth rate for the ITG-dominant region, whereas the difference is marginal for TEM-dominant cases.

To further investigate the characteristics of CTEM instability using the extended model, I have run more linear simulations using the same Cyclone parameters as Fig. 3.1 except for $a = 0.666$ m, $R_0 = 1.86$ m, and $R_0/L_{Ti} = 2.22$ to look at TEM-dominant cases. The extended model shows a considerable difference when magnetic shear $\hat{s}$ is varied across 0 because deeply trapped approximation fails to capture the precession reversal exist at weak shear. This is demonstrated in Fig. 3.2. k_θ scan result (Fig. 3.3) with $\hat{s} = 0.1$ shows that TEM instability is dominant under these parameters. It also shows that the extended model has reduced growth rate compared to the old model, especially at higher k_θ.

Next, I perform a magnetic shear scan in $\hat{s} = -0.4 \sim 1.5$ at $r = 0.5a$. The results of real frequency ω_r and growth rate γ are shown in Figs. 3.4 and 3.5. As shown in Fig. 3.4, real frequency ω_r shows only little difference between the two models. The extended model shows reduction in growth rate in $\hat{s} = 0 \sim 1.2$, by up to 20 %. The linear increase in $\omega_r(\hat{s})$ in both models and a slight concave

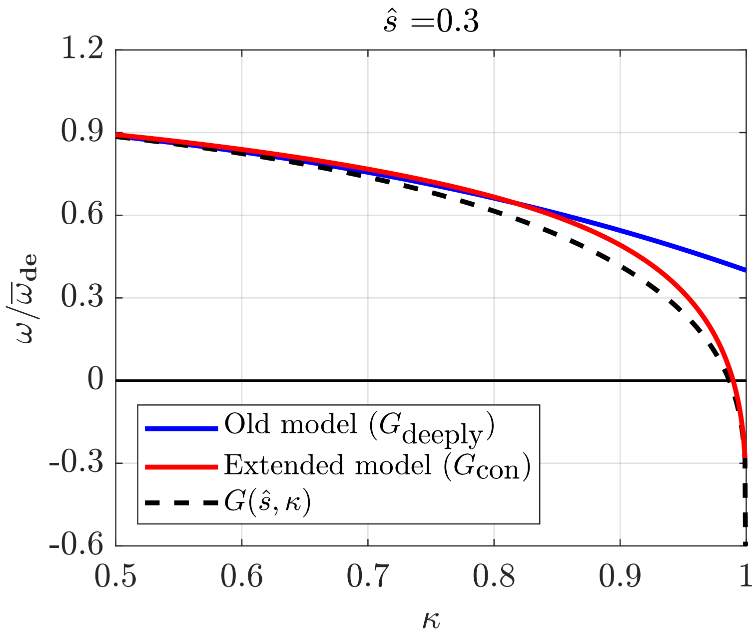

Figure 3.2 Precession drift frequency ω normalized by $\overline{\omega}_{de}$ in the old model (blue) and in the extended model using connection formula (red), compared to its theoretical value (black).

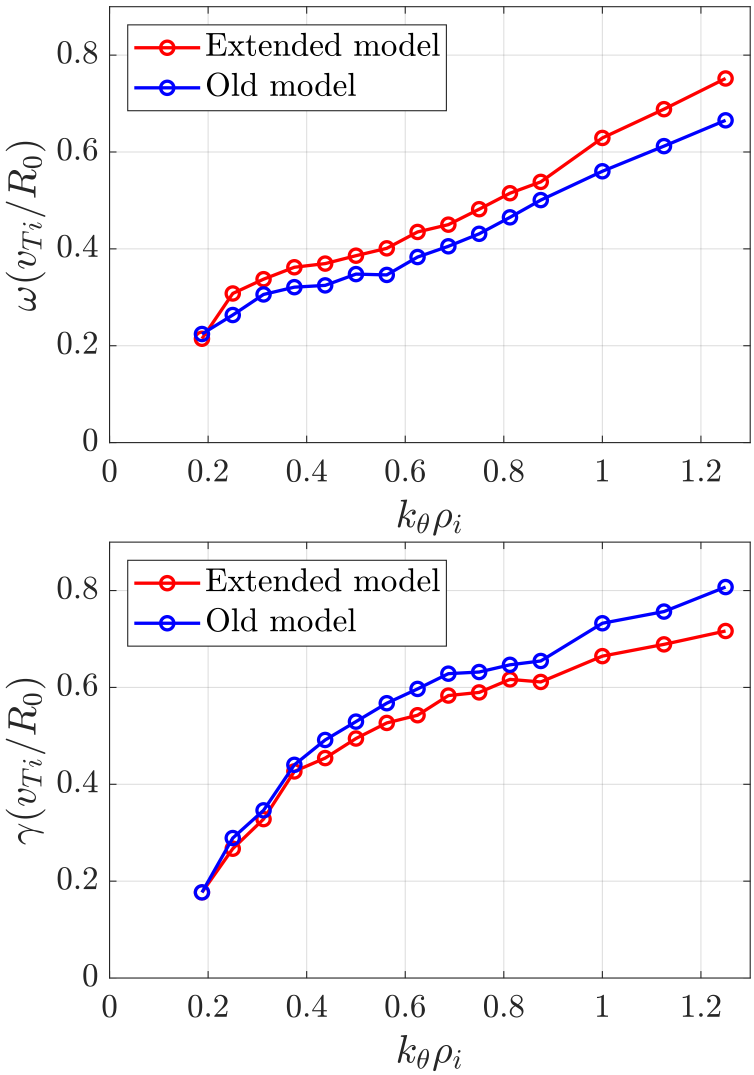

Figure 3.3 The real frequency ω_r (top) and the growth rate γ (below) of TEM instability in TEM dominated case with $R_0/L_{Ti} = 2.22$.

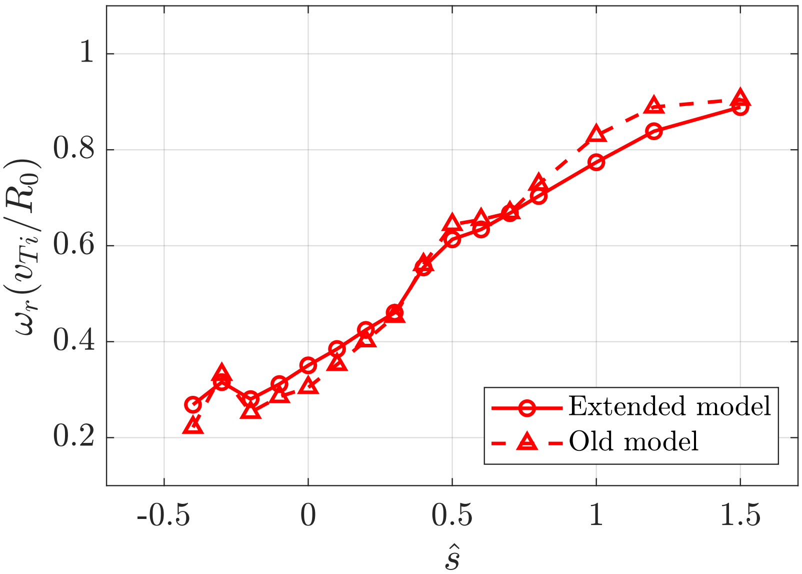

Figure 3.4 Magnetic shear $\hat{s}$ scan of the real frequency ω_r in reversed shear plasma using the extended model (solid line) and using the old model (dashed line).

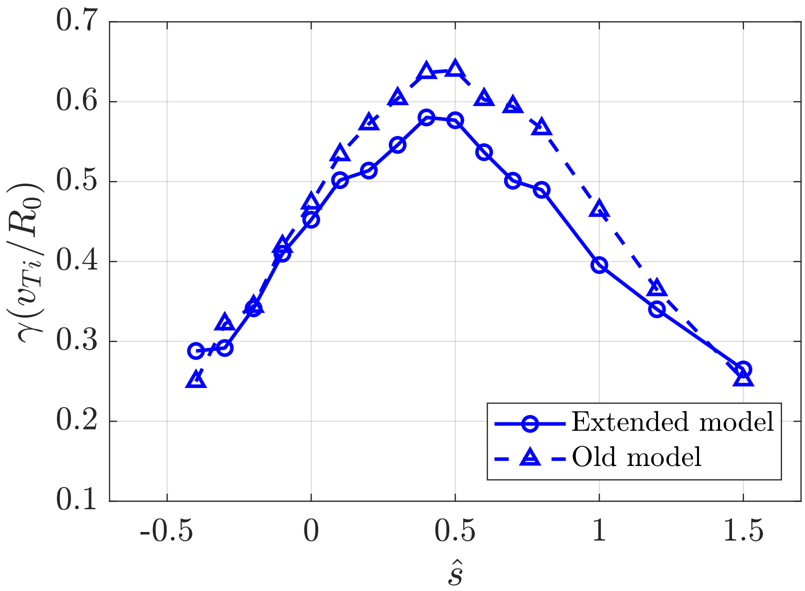

Figure 3.5 Magnetic shear $\hat{s}$ scan of the growth rate γ in reversed shear plasma using the extended model (solid line) and using the old model (dashed line).

downwards shape of $\gamma(\hat{s})$ in $\hat{s} = -0.4 \sim 0.5$ for the extended model matches well with CTEM calculations using kinetic electrons [40]. The reduction of the growth rate in the extended model for $\hat{s} = 0 \sim 1.2$ can be attributed to the old model's poor representation of precession reversal for barely trapped particles, as shown in Fig. 3.2.

At negative magnetic shear of $\hat{s} = -0.4 \sim 0$, the stabilizing effect of barely trapped electrons is insignificant. This rather counter-intuitive result can be understood as follows. From the bounce-averaged gyrokinetic theory, the TEM growth rate is determined from the resonance term between the precession drift and the electron diamagnetic drift [41]. The precession-reversed electrons do not resonance with the TEM, which has an opposite sign of phase velocity. When magnetic shear is strongly negative, most trapped particles except for the deeply trapped ones have fast reversed precession, and the old model using deeply trapped approximation is sufficiently accurate to describe particles with the positive precession direction. Thus, despite the two models with drastically different precession frequency for barely trapped particles, the TEM instability is quite insensitive to such difference for strongly negative shear and shows no difference in γ.

Figure 3.6 shows mode structures of TEM turbulence in the old model and in the extended model. The two models share a very similar mode structure, but eigenmode shapes are a bit different. The mode amplitude maximum position for the extended model is around the center with $r/a = 0.5$ and $R/R_0 = 1.17$, where electron temperature gradient is maximum. In contrast, the amplitude maximum is located further outside for the old model, at around $R/R_0 = 1.20$. This result implies that in reversed shear plasmas, stabilizing influence due to barely trapped particles' reversed precession is as important as that of electron temperature gradient around q_{min}. Hence, the extended model can lead to a more realistic description of TEM instability. In nonlinear simulations where nonlinear mode interaction is significant and their interaction persists in the time scale as long as confinement time, improvements provided by the extended model may lead to a more accurate description of TEM turbulence properties such as thermal transport.

3.3 Nonlinear gyrokinetic simulation results

In this section, I analyze nonlinear simulation results using the extended model and the old model. In Sec. 3.2, the linear simulations showed a clear trend of reduction in growth rate under weak magnetic shear ($0 < \hat{s} < 1.2$), albeit by a small amount. This may suggest that nonlinear simulation results between

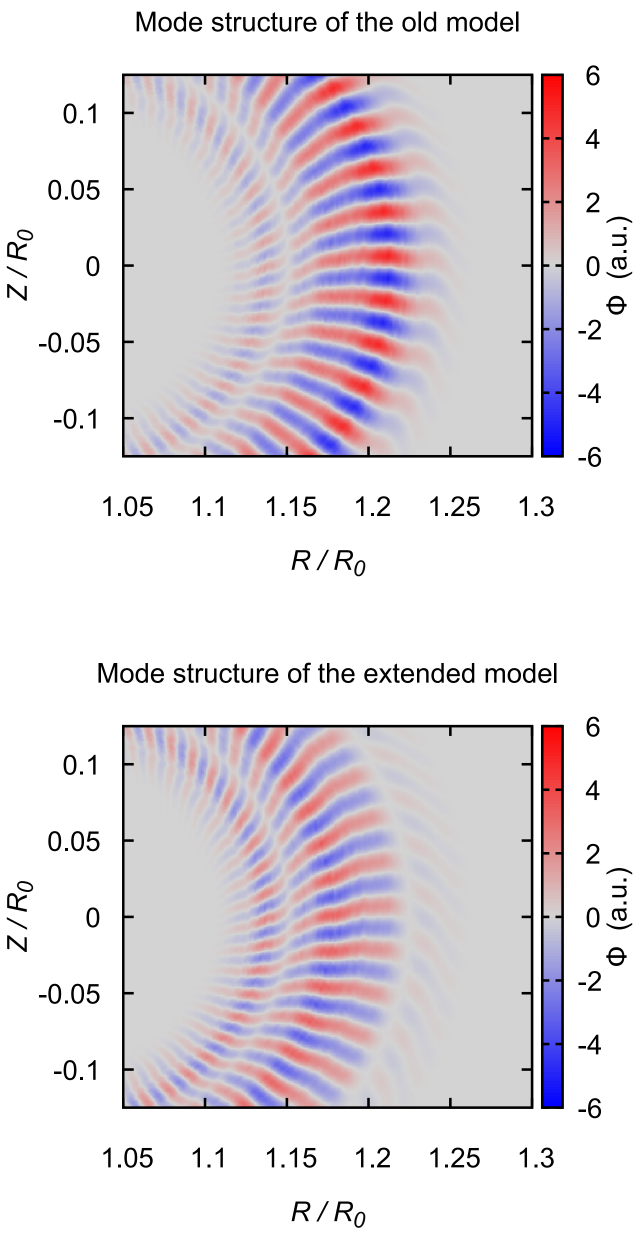

Figure 3.6 TEM electric potential ϕ mode structure in the old model (top) and in the extended model (below) from the linear simulations. Here, R and Z are horizontal position and vertical position normalized by R_0, respectively.

two models would be similar aside from minor difference in growth rate. To check this conjecture, I study nonlinear simulations of two CTEM unstable plasmas which are suspected to show the most clear difference based on the linear simulation results. The first one is the reversed shear (RS) plasma. As argued in Sec. 2.4, the difference in precession motion between the two models is the most significant when $\hat{s}$ is near 0. Reversed shear plasmas which typically have $-0.5 < \hat{s} < 0.5$ in core plasma meet such criteria. However, the results from Sec. 3.2 suggest that magnetic shear values of $0 < \hat{s} < 1.2$ show larger difference of growth rate than weakly negative magnetic shear. Hence, the other plasma uses magnetic shear profile relevant for hybrid scenario plasmas, which has $0 < \hat{s} < 1$ in the core plasma [42, 43], and will be referred to as the hybrid scenario (HS) plasma. Aside from safety factor q and magnetic shear $\hat{s}$, all the other parameters such as temperature gradients are identical to the ones used in magnetic shear scan of linear growth rate, from Sec. 3.2, with their initial profiles shown in Fig. 3.7. Density and temperature profiles are exponential in $0.3a < r < 0.7a$, i.e., their gradient lengths are constant. The safety factor and magnetic shear profile used for two plasmas in nonlinear simulations are shown in Figs. 3.8 and 3.9, respectively. In the nonlinear simulations, I use 40 toroidal modes $n = 0 \sim 156$ which correspond to $k_\theta \rho_i = 0 \sim 2.4$, so that the most unstable mode and the higher modes are included. Time step size is $\Delta t = 0.02 R_0 / v_{Ti}$, radial grid number is $N_x = 200$, and the number of marker particles per mode is 1920 for ions and 384 for electrons.

Electric potential plots from the reversed shear and the hybrid scenario plasmas using the extended model after nonlinear saturation are shown in Figs. 3.10 and 3.11. In nonlinear gyrokinetic simulation of microinstabilities such as ITG and TEM, exponential growth of instability eventually reach saturation due to mode interaction. For the reversed shear plasma, eigenfunction maxima is

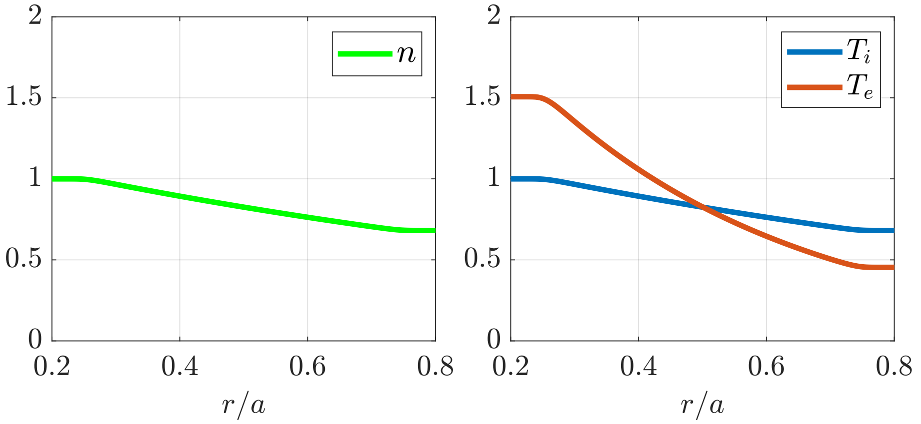

Figure 3.7 Initial profiles of density n, ion temperature T_i, and electron temperature T_e, normalized by their values at $r = 0.5a$.

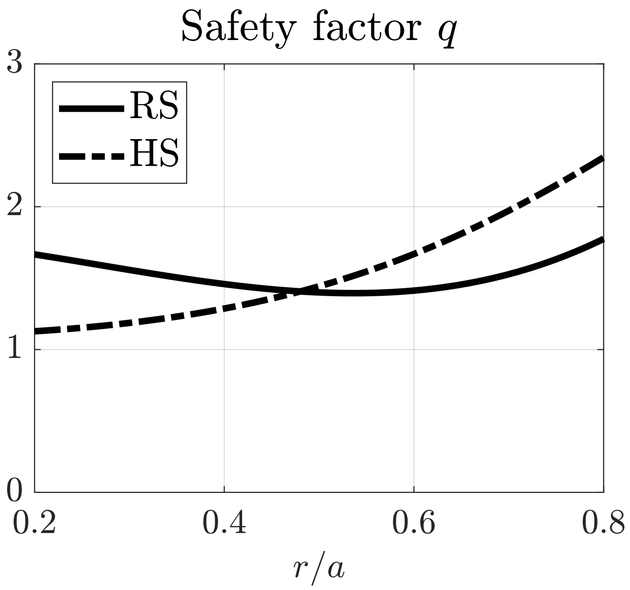

Figure 3.8 Safety factor q profiles used in nonlinear simulations for reversed shear (RS) plasma in solid line and hybrid scenario (HS) plasma in dashed line.

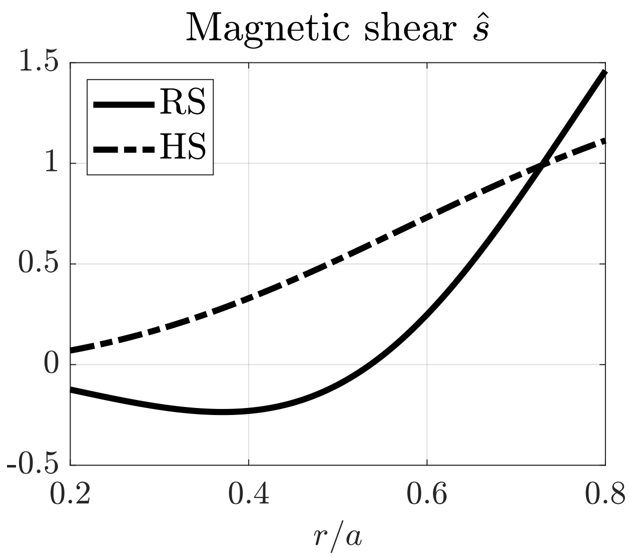

Figure 3.9 Magnetic shear $\hat{s}$ profiles used in nonlinear simulations for reversed shear (RS) plasma in solid line and hybrid scenario (HS) plasma in dashed line.

around $r = 0.6a$ and for the hybrid scenario, $r = 0.4a$. When compared with magnetic shear profiles in Fig. 3.9, both points roughly correspond to where $\hat{s} \sim 0.4$ in which linear growth rate has its maximum value for both models (Fig. 3.5). In terms of the bounce-kinetic models used, there were no significant difference in mode structure between the two models. Time evolution of potential at mode structure maximas from reversed shear plasma and hybrid scenario plasma are shown in Figs. 3.12 and 3.13, respectively. In these figures, the growth rate differences are $\sim$ 11% for reversed shear plasma and $\sim$ 14% for hybrid scenario plasma. These quantities are roughly in line with the linear simulations, where the extended model yields up to $\sim$ 20% of reduced growth rate.

Heat flux results show a more clear difference between the two models. The spatiotemporal evolution of heat flux in the reversed shear plasma is shown

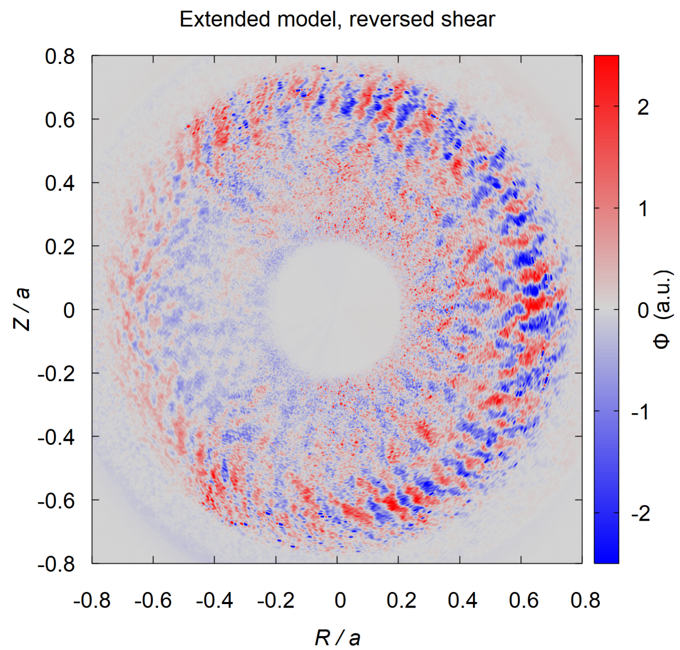

Figure 3.10 Mode structure of the perturbed electric potential from the reversed shear plasma at $t = 150R_0/v_{Ti}$ when nonlinear saturation is established, using the extended model.

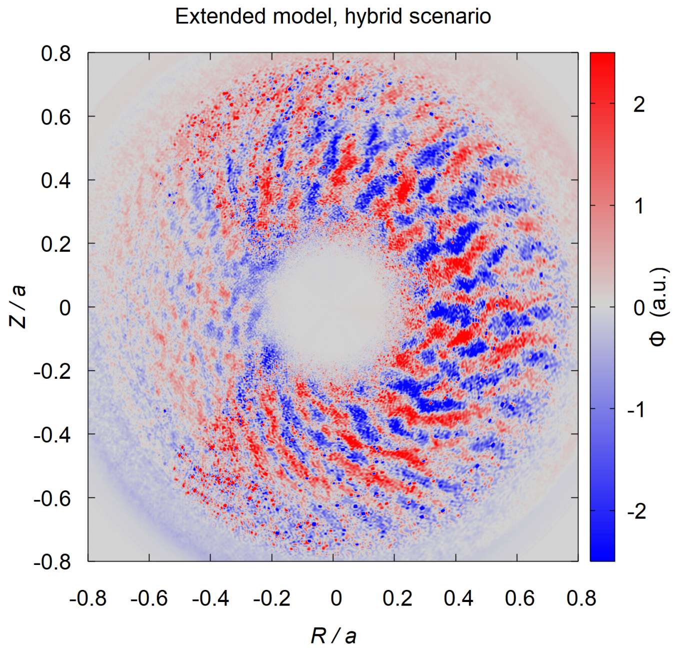

Figure 3.11 Mode structure of the perturbed electric potential from the hybrid scenario plasma at $t = 150R_0/v_{Ti}$ when nonlinear saturation is established, using the extended model.

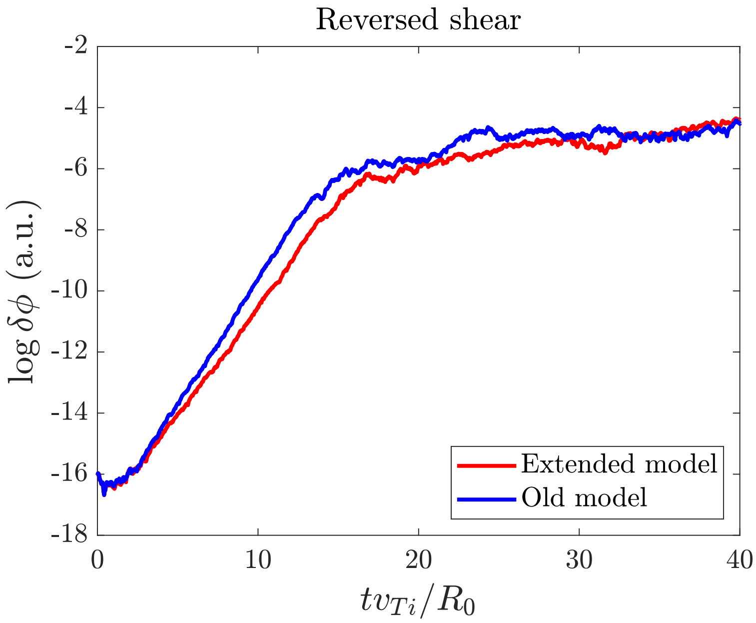

Figure 3.12 Time evolution of the perturbed electron potential $\delta\phi$ in reversed shear plasma at mode structure maxima ($r = 0.6a$) using the extended model (red) and using the old model (blue).

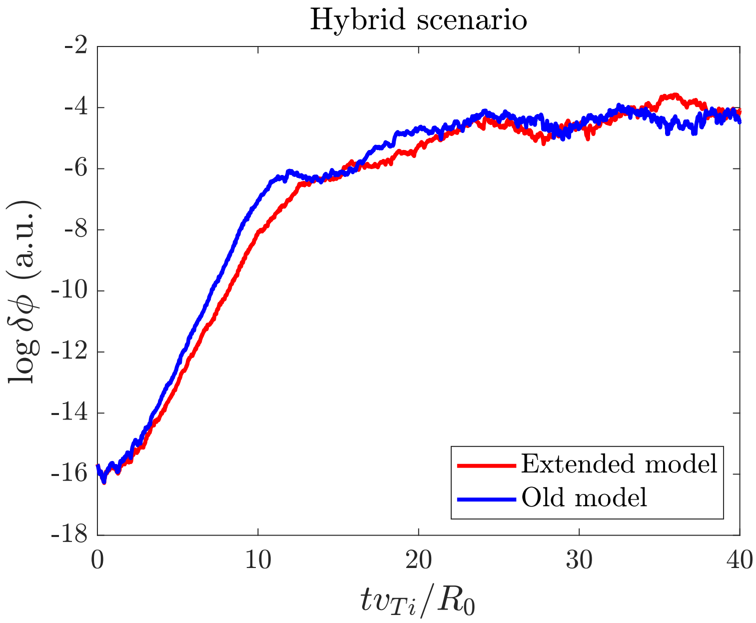

Figure 3.13 Time evolution of the perturbed electric potential $\delta\phi$ in hybrid scenario plasma at mode structure maxima ($r = 0.4a$) using the extended model (red) and using the old model (blue).

in Fig. 3.14. Here, heat flux level is higher in the old model, especially at the beginning of nonlinear saturation ($t \sim 42R_0/v_{Ti}$). Time evolution of heat flux at $r = 0.58a$ where TEM is the most unstable, is plotted in Fig. 3.15. I set $t = 80R_0/v_{Ti}$ as the time when the nonlinear saturation effect starts to plateau. In this figure, before $t = 80R_0/v_{Ti}$, the heat flux is reduced by $\sim 22\%$ in the extended model and after $t = 80R_0/v_{Ti}$, heat flux is reduced by $\sim 14\%$ in the extended model. For the hybrid scenario plasma (Fig. 3.16), the difference in heat flux at the most unstable spot, $r = 0.42a$, is not as apparent as shown in Fig. 3.17. Before $t = 80R_0/v_{Ti}$, the extended model shows $\sim 4\%$ more heat flux and after $t = 80R_0/v_{Ti}$, about 6% more. In summary, despite the linear and nonlinear simulation results of electric potential suggesting that difference between two models would be more apparent in the hybrid scenario plasma, in the case of heat flux, meaningful difference between the models exist only for the reversed shear plasma.

To further compare two models in nonlinear simulation, I analyze radial electric field results. In the simulation, radial electric field is calculated from zonal potential $\phi_{0,0}$ as $E_r = \dfrac{\partial \phi_{0,0}}{\partial r}$. Radial electric field results from the nonlinear simulations are shown in Fig. 3.18 and Fig. 3.19. Note that the result is time-averaged in $t = 144R_0/v_{Ti} \sim 156R_0/v_{Ti}$ for both plasmas. In the results, radial electric field profiles after nonlinear saturation change very slowly over time and their time dependency is negligible. In the reversed shear plasma, as shown in Fig. 3.18, radial electric field is much higher in the old model whereas the profile shape is similar. For the hybrid scenario plasma, the difference between the two models is not very clear. The lack of significant difference between two models is in line with the heat flux result from hybrid scenario plasma. However, it requires further work as to discuss how reduction in radial electric field and correspondingly $E \times B$ shear can lead to suppressed heat transport. This

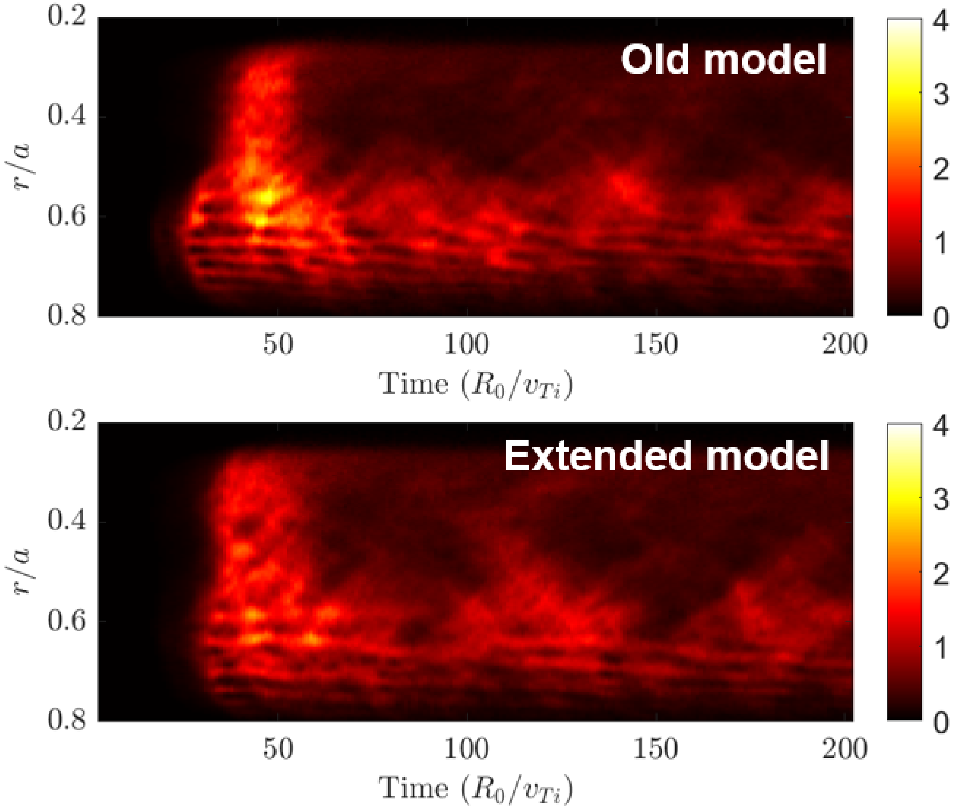

Figure 3.14 Spatiotemporal evolution of heat flux using the old model (above) and the extended model (below) in the reversed shear plasma.

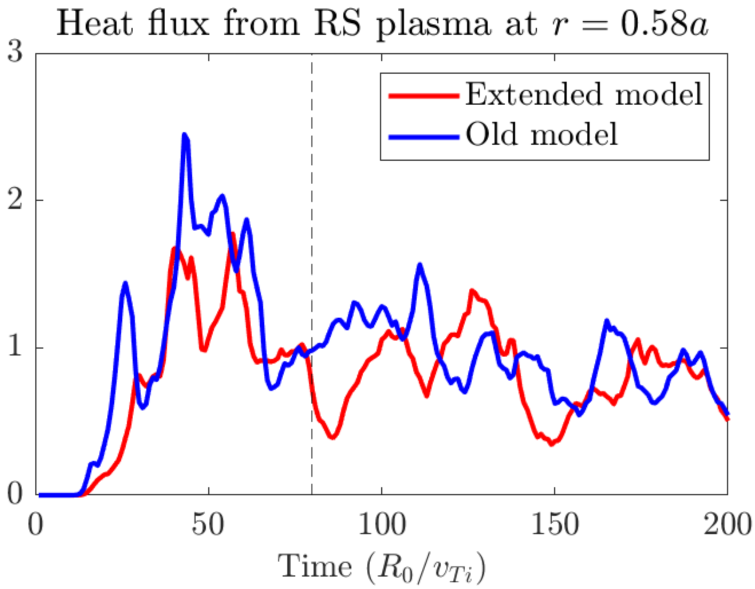

Figure 3.15 Time evolution of heat flux in the reversed shear plasma at the mode maxima ($r = 0.58a$) using the old model in blue line and using the extended model in red line. Dashed lines indicate $t = 80R_0/v_{Ti}$ when the nonlinear saturation effect starts to plateau.

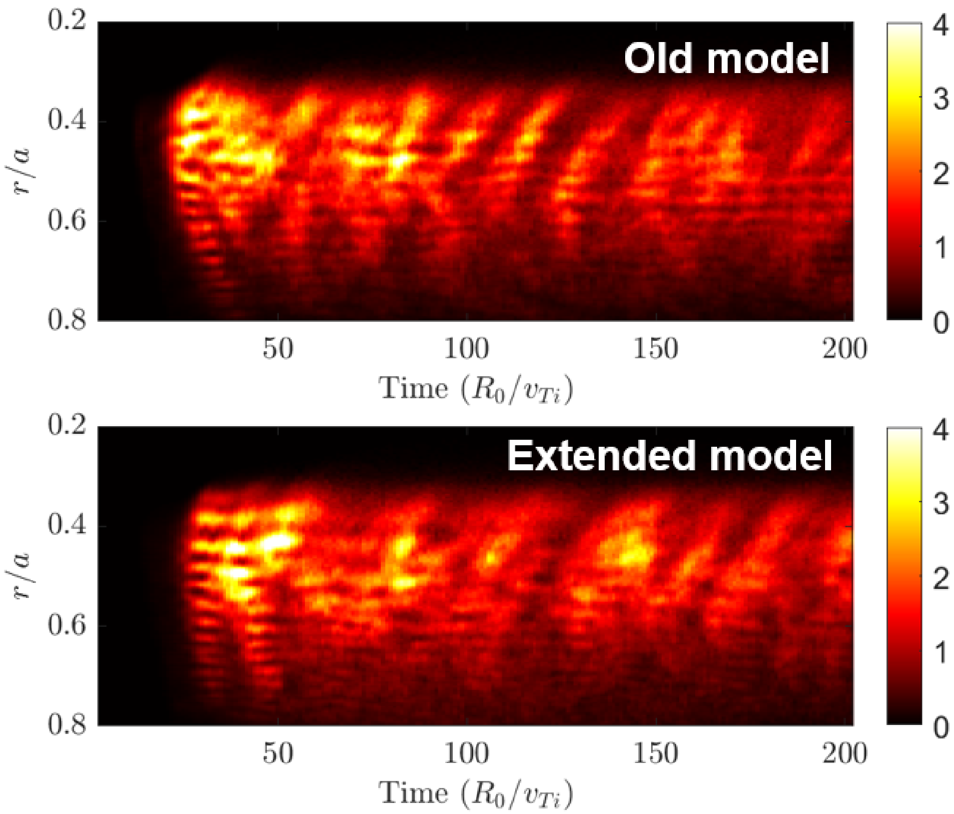

Figure 3.16 Spatiotemporal evolution of heat flux using the old model (above) and the extended model (below) in the hybrid scenario plasma.

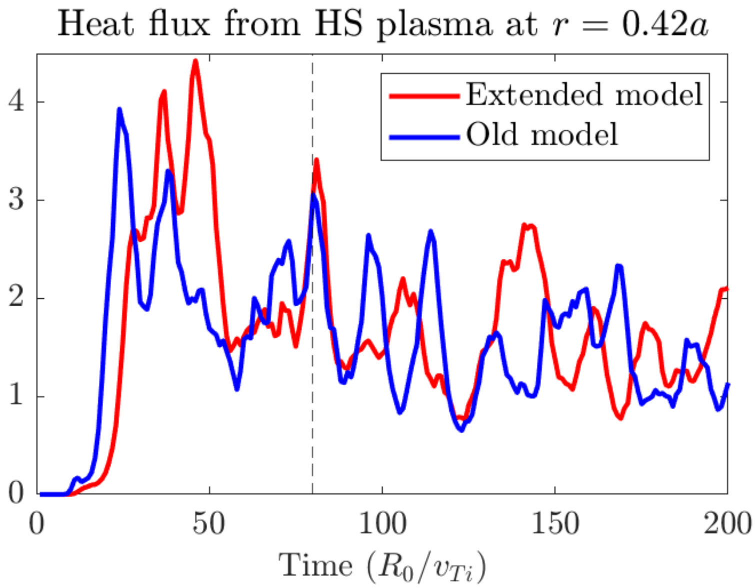

Figure 3.17 Time evolution of heat flux in the hybrid scenario plasma at the mode maxima ($r = 0.58a$) using the old model in blue line and using the extended model in red line. Dashed lines indicate $t = 80R_0/v_{Ti}$ when the nonlinear saturation effect starts to plateau.

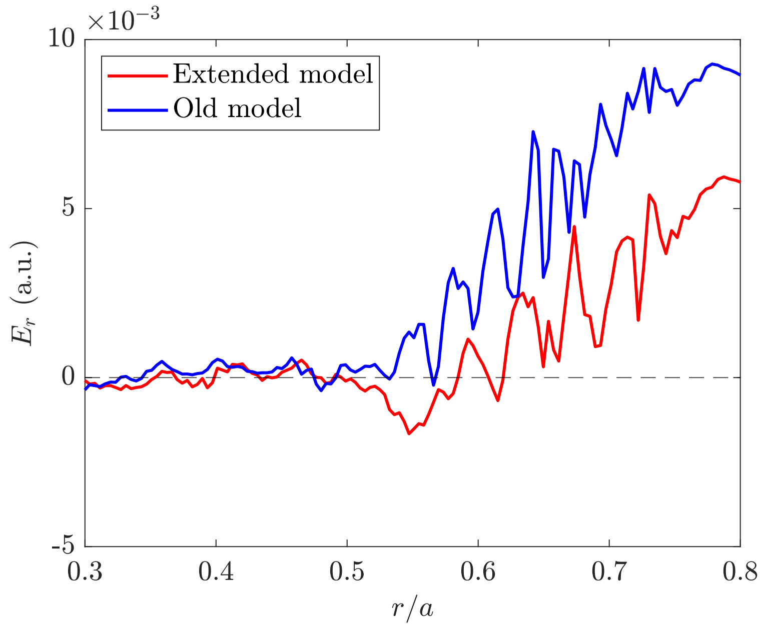

Figure 3.18 Radial electric field E_r in the reversed shear plasma at $r = 0.58a$, averaged in $t = 144R_0/v_{Ti} \sim 156R_0/v_{Ti}$.

remains as a future work.

Nonlinear simulation results highlight the extended model's capability to accurately calculate barely trapped particle dynamics. Extending the equations of motion (Eq. 2.2) for barely trapped particles change how bounce orbits travel in the binormal direction, i.e. it changes $\frac{d\alpha}{dt}$. This is demonstrated in Fig. 2.3, where at $\hat{s} = 0.5$ and $\hat{s} = 1$, barely trapped particles with $\kappa \sim 1$ show lower $\frac{d\alpha}{dt}$ in the extended model. This could meaningfully reduce heat transport when barely trapped particle effects are significant, suggesting that the trend of transport reduction shown in Fig. 3.15 is due to barely trapped electrons.

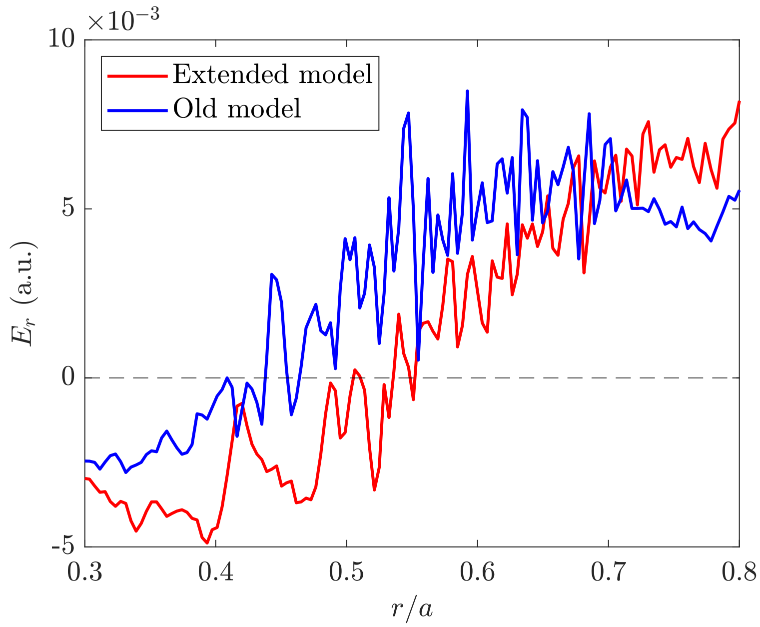

Figure 3.19 Radial electric field E_r in the hybrid scenario plasma at $r = 0.42a$, averaged in $t = 144R_0/v_{Ti} \sim 156R_0/v_{Ti}$.

Chapter 4

Discussions

So far, I have discussed that the extended model can accurately describe trapped particles dynamics by including the effects of barely trapped particles, through its better estimation of CTEM linear growth rate, heat flux, and zonal flow. In this section, I present applications and future works of the extended model.

One possible application is internal transport barrier (ITB) research using bounce-kinetics. ITBs in fusion plasma enable enhanced confinement regime by creating a stiff pressure gradient layer with suppressed transport. Studies have shown that turbulence suppression from negative magnetic shear [44, 45] and strong $E \times B$ flow shear are favorable for ITB formation. In a recent work, ITB formation in reversed shear plasma has been observed from gyrokinetic simulations using hybrid electrons, and the authors have found that counter rotation of TEM turbulence is favorable for the formation of ITB [46]. Hybrid electron regime which assumes adiabatic response for non-zonal passing electrons and treats the rest as fully kinetic electrons [47] saved computing cost considerably and enabled the authors to conduct nonlinear flux-driven simulation while retaining the trapped electron physics. The extended bounce kinetic model provides a more efficient numerical model by using further reduction of dimensionality, thus can be used in gyrokinetic simulations of ITB formation where TEM plays a significant role.

It is possible to develop the extended model for general geometry in principle. So far, bounce action and bounce frequency formulas in bounce-kinetics all have assumed circular high aspect ratio tokamak [15, 16]. However, the general bounce-kinetic model is written in flux coordinates and is valid for any tokamak geometries. One can further develop the extended model using the general forms of J_b and ω_b [48] and apply them in other geometries. To do this, J_b and ω_b are written as functions of mutually dependent parameter κ, which indicate "trapped-ness", so that ω_b as a function of J_b is independent with κ in both deeply trapped and barely trapped limits. Then, Hamiltonian and Hamilton's equations are written as functions of flux coordinates and adiabatic invariants in respective limits. For example, one can follow geometries used by Xiao and Catto [49] or Roach et al. [50]. After getting the expression for Hamiltonian, the result can be verified by following similar steps as Sec. 2.4.

Another application suitable for the extended model is trapped fast particle effects on microturbulence. Recently, fast ion stabilization of ITG turbulence due to wave-particle resonance has been reported [51, 52]. This has been explained in the analytic study using bounce-kinetic theory by Wang et al. [53] where the authors showed that fast ions with precession drift along ion diamagnetic direction resonate stabilize ITB turbulence. On the other hand, fast ions in reversed shear plasma with reversed precession can destabilize electron drift wave [54, 55]. These trapped fast ion effects can be studied in gyrokinetic simulations using the extended model, and one can explore their roles in long-time nonlinear simulations, ultimately in reactor plasmas.

Limitations exist in the current bounce-kinetic model implemented in gKPSP, as electromagnetic effects have not been included. The feasibility of expanding bounce-kinetics for electromagnetic perturbations has been addressed in Ref. 3. However, deriving explicit forms of generating functions and the coordinate transforms which are necessary to build a numerical model have not been done to date. If the extended bounce-kinetic model's capability is expanded to include the electromagnetic effects, the extended model can explore the effects of various low frequency MHD modes on transport in gyrokinetic simulations. For example, one can study energetic particle mode (EPM) driven by the precession of trapped energetic particles [56] or the electron fishbones driven by barely trapped supra-thermal electrons [57].

Chapter 5

Conclusion

In this thesis, I have developed the extension of the bounce-kinetic model that can properly describe barely trapped particles. Using the extended model, I have performed collisionless TEM simulations using the gKPSP gyrokinetic code. Compared to the old model, the extended model yields a reduction in the TEM linear growth rate for low magnetic shear due to the reversed precession of barely trapped electrons. In the nonlinear simulations of TEM instability, the extended model yields lower heat transport and lower radial electric field in the reversed shear plasma, likely due to modifications for the barely trapped particle motions. The results exhibit that the extended model is capable of properly treating barely trapped particles, and more accurate simulations of TEM turbulence, in particular for low magnetic shear. The extended model can provide a new and efficient way of properly studying trapped particle effects in the reversed shear plasmas and low magnetic shear hybrid scenario [42, 43] plasmas. Several applications were discussed, including studying the effects of trapped fast particles [51, 54] and studying ITB formation in the presence of TEM [46]. Further advancement of the bounce-kinetic theory to include electromagnetic effects will enable the extended model to properly study some low-frequency MHD modes driven by trapped particles [56,57]. Wide adoption of the extended model can help to efficiently simulate the long-time evolution of turbulence physics while attaining the kinetic response of the trapped particles and the physical rigor that modern gyrokinetics provides, and ultimately help reveal the mysteries of fusion plasma turbulence.

Bibliography

[1] E. A. Frieman and Liu Chen, Phys. Fluids **25**, 502 (1982).

[2] T. S. Hahm, Phys. Fluids **31**, 2670 (1988).

[3] A. J. Brizard and T. S. Hahm, Rev. of Modern Phys. **79**, 421 (2007).

[4] Z. Lin, *et al.*, Science **281**, 1835 (1998).

[5] X. Garbet, *et al.*, Nucl. Fusion **50**, 043002 (2010).

[6] T. S. Hahm *et al.*, Plasma Phys. Conrol. Fusion **46**, A323 (2004).

[7] O. D. Gurcan *et al.*, Phys. Plasmas **13**, 052306 (2006).

[8] S. Yi *et al.*, Nucl. Fusion **55**, 092002 (2015).

[9] P. A. Politzer, Phys. Rev. Lett. **84**, 1192 (2000).

[10] S. J. Zweben *et al.*, Phys. Plasmas **9**, 1981 (2002).

[11] M. J. Choi *et al.*, Nucl. Fusion **59**, 086027 (2019).

[12] G. Dif-Pradalier *et al.*, Phys. Rev. Lett. **114**, 085004 (2015).

[13] G. Hornung *et al.*, Nucl. Fusion **57**, 014006 (2017).

[14] G. Dif-Pradalier *et al.*, Nucl. Fusion **57** 066026 (2017).

[15] B. H. Fong and T. S. Hahm, Phys. Plasmas bf 6, 188 (1999).

[16] Lu Wang and T. S. Hahm, Phys. Plasmas **16**, 062309 (2009).

[17] Y. Idomura, *et al.*, J. Plasma Fusion Res. Ser. **6**, 17 (2004).

[18] Lei Qi *et al.*, Phys. Plasmas **23**, 062513 (2016).

[19] J. M. Kwon *et al.*, Comp. Phys. Comm. **215**, 81 (2017).

[20] F. -X. Duthoit *et al.*, Phys. Plasmas **21**, 122510 (2014).

[21] Y. W. Cho and T. S. Hahm, Nucl. Fusion **59**, 066026 (2019).

[22] Y. W. Cho and T. S. Hahm, Phys. Plasmas 28, 052303 (2021).

[23] G. Depret *et al.*, Plasma Phys. Control. Fusion **42**, 949 (2000).

[24] T. S. Hahm and W. M. Tang, Phys. Plasmas **3**, 242 (1996).

[25] A. Ghizzo *et al.*, Phys. Plasmas **17**, 092501 (2010).

[26] Y. Idomura *et al.*, J. Plasma Fusion Res. **75**, 131 (1999).

[27] T. Drouot *et al.*, Eur. Phys. J. D **68**, 280 (2014).

[28] B. B. Kadomtsev and O. P. Pogutse, Sov. Phys. JETP **24**, 1172 (1967).

[29] R. G. Littlejohn, J. Math. Phys. **23**, 742 (1982).

[30] J. R. Cary and R. G. Littlejohn, Ann. Phys. (NY) **151**, 1 (1983).

[31] B. C. Carlson, "Elliptic Integrals", in NIST Handbook of Mathematical Functions (Cambridge University Press, Cambridge, 2010), Chap. 19.

[32] R. Roy and F. W. J. Oliver, “Elementary Functions”, in NIST Handbook of Mathematical Functions (Cambridge University Press, Cambridge, 2010), Chap. 4.

[33] F. Y. Gang and P. H. Diamond, Phys. Fluids B **2**, 2976 (1990).

[34] J. M. Kwon *et al.*, Nucl. Fusion **52**, 013004 (2012).

[35] Lei Qi *et al.*, Nucl. Fusion **59**, 026013 (2019).

[36] Lei Qi *et al.*, Nucl. Fusion **61**, 026010 (2021).

[37] Y. Idomura, J. Comput. Phys. **313**, 511 (2016).

[38] A. M. Dimits *et al.*, Phys. Plasmas **7**, 969 (2000).

[39] G. Rewoldt *et al.*, Comp. Phys. Comm. **177**, 775 (2007).

[40] Jiquan Li and Y. Kishimoto, Plasma Phys. Control. Fusion **44**, A479 (2002).

[41] J. C. Adam *et al.*, Phys. Fluids **19**, 561 (1976).

[42] F. Turco *et al.*, Phys. Plasmas **22**, 056113 (2015).

[43] Yong-Su Na *et al.*, Nucl. Fusion **60**, 086006 (2020).

[44] P. H. Diamond *et al.*, Phys. Rev. Lett. **78**, 1472 (1997).

[45] T. S. Hahm, Plasma Phys. Control. Fusion **44**, A87 (2002).

[46] K. Imadera and Y. Kishimoto, 28th IAEA-FEC, TH/4-5

[47] E. Lanti *et al.*, J. Phys.: Conf. Ser. **1125**, 012014 (2018).

[48] A. J. Brizard, Phys. Plasmas **7**, 3238 (2000).

[49] Y. Xiao and P. Catto, Phys. Plasmas **13**, 082307 (2006)

[50] C. M. Roach *et al.*, Plasma Phys. Control. Fusion **37**, 679 (1995).

[51] A. Di Siena *et al.*, Nucl. Fusion **58**, 054002 (2018).

[52] A. Di Siena *et al.*, Phys. Plasmas **26**, 052504 (2019).

[53] S. Wang *et al.*, Plasma Sci. Technol. **24**, 065102 (2022).

[54] B. J. Kang and T. S. Hahm, Phys. Plasmas **26**, 042501 (2019).

[55] B. J. Kang *et al.*, Phys. Plasmas **27**, 072510 (2020).

[56] L. Chen, Phys. Plasmas **1**, 1519 (1994).

[57] F. Zonca *et al.*, Nucl. Fusion **47**, 1588 (2007).

초록

비선형 bounce 동역학적 이론을 따르는 bounce 평균된 동역학 모델 은 이미 여러 수치모사 연구에 적용된 바 있다. 본 학위논문은 간신히 갇힌 입자들에 대해서도 올바른 계산을 수행할 수 있도록 기존 모델을 개량한, 연장된 bounce 동역학 모델에 대해 보고하며 gKPSP 시뮬레이션에 이를 적용한 결과를 소개한다. Bounce-gyrocenter 좌표계의 단열불변량들에 대한 함수로 표현된 갇힌 입자의 Hamiltonian을 유도하고, 세차 드리프트에 관한 기존 식과 비교하여 결과를 검증한다. 새롭게 개발된 모델은 낮은 자기장 전단을 갖는 플라즈마에서 비충돌성 갇힌 전자 모드 (CTEM) 에 대한 gyrokinetic 전산모사에 적용했을 때 더 정확한 결과를 얻었다. 새로운 모델은 낮은 자기장 전단을 갖는 플라즈마의 선형 시뮬레이션에서 더 낮은 성장률을 보였고 역전된 자기장 전단을 갖는 플라즈마의 비선형 시뮬레이션에서는 더 낮은 열류속과 더 낮은 반지름 방향 전기장을 나타냈다. 마지막으로, 연장된 bounce 동역학 모델의 적용 분야에 대해 논의한다.

주요어: 핵융합 플라즈마, 토카막, 난류, gyrokinetic 전산모사, bounce 동역학론, 갇힌 전자 모드

학번: 2018-26018

감사의 글

먼저, 지도교수이시며 학문적 엄밀함에 있어 본보기이신 함택수 교수님께 감사의 말씀을 전합니다. 함께 생활하며 저의 곁에서 응원해주고 많은 도움을 준 강병준 선배, 조영우 선배, 그리고 최경진 선배에게 감사합니다. 또한, 저의 대학 및 대학원 생활에 큰 힘이 되어준 제 가족에게 감사의 말씀을 전합니다. 마지막으로, 고마움을 표현하지 못했지만 큰 보탬이 되어준 소중한 인연들에게 감사의 뜻을 표합니다.